

Quantum-Efficiency Enhancement and Mechanical Responsiveness of Solid-State Photoluminescence Materials Based on Uniaxial Cellulose Nanocrystal Arrays in Flexible Polymer via Assembly-Induced Emission

Siyuan Liu

Southwest University

Zhenxu Shi

Southwest University

Xuhong Wang

Southwest University

Yanbin Gong

Wuhan University

Xijun Li

Chengdu Banknote Printing Co., Ltd.

Xin Jia

Shi He Zi University: Shihezi University

Lin Gan

Southwest University

Jin Huang (✉ huangjin@iccas.ac.cn)

Southwest University <https://orcid.org/0000-0003-0648-2525>

Research Article

Keywords: Cellulose nanocrystals, Poly (vinyl alcohol), Uniaxial assembly, Mechanical responsiveness, Luminescence enhancement

Posted Date: September 30th, 2021

DOI: <https://doi.org/10.21203/rs.3.rs-630237/v1>

License: © ⓘ This work is licensed under a Creative Commons Attribution 4.0 International License.

[Read Full License](#)

Abstract

Assembling cellulose nanocrystals (CNCs) can induce solid-state photoluminescence based on Stokes scattering. Such photoluminescence is free of photo-quenching and should have great potential in optical materials, whereas poor flexibility of assembled CNC arrays limits its applications. Here, a co-assembly of binary components including 1D nanoparticles and long-chain polymers had been explored to introduce the uniaxial CNC arrays into a transparent poly (vinyl alcohol) (PVA) membrane, which enhanced the mechanical properties, especially the stretchable property. Besides, the CNC assembly was controlled by adjusting the volume ratio between CNC and PVA. The result indicated that co-assembly with PVA could improve the uniaxial orientation of assembled CNC arrays, which played a crucial role in enhancing the emission quantum-efficiency (EQE) of CNC. Stretching the PVA/CNC membrane could furthermore induce an enhancement in EQE together with a gradual shift in emission wavelength. The mechanism study on that stimulation-response suggested that the enhancement and shift came from the change in the uniaxial orientation degree and periodicity of the CNC assembly, respectively. Since the stimulation-responsive enhancement in EQE (from ca. 40% to ca. 60%) can even be observed by naked eyes, we believe such cellulose-based materials can be widely used in optical sensors.

Introduction

Periodic assembly structures with structural colors have great potential in optical sensors (Wu et al. 2019, Zhao et al. 2017), anti-counterfeiting (Chu et al. 2019), and information security (Yang et al. 2019). Unlike pigments or fluorescent materials, the structural colors do not fade and are free of photo-bleaching (Echeverri et al. 2019, Wang et al. 2019, Zhang et al. 2019). The brightness and color of those assembly structures can also be adjusted via controlling their periodicity and orientation (Tong et al. 2016, Gu et al. 2016). Meanwhile, the uniaxial assembly membrane of rod-like cellulose nanocrystals (CNCs) was recently found to own not only structural colors but also a property of assembly-induced emission (Gan et al. 2019). The length of CNC could then be adjusted via choosing a suitable cellulose resource, and then the optical information of the assembly membrane could hide in visible light.

However, the low toughness of CNC membranes from the low flexibility of CNC has limited the application of its uniaxial assembly structure in optical sensors. Fortunately, CNC could assemble in flexible matrices to enhance the mechanical properties of CNC membranes (Shopsowitz et al. 2012, Guidetti et al. 2016, Leng et al. 2018). Also, CNCs could self-assemble in the polymer precursors and form flexible hydrogel with structural color after polymerization (Kelly et al. 2013, Khan et al. 2013). Those materials might further display different structural colors when stimulated by strain (Giese et al. 2013), humidity (Khan et al. 2015, Yao et al. 2017), and solvent (Giese et al. 2014), which made CNC assembly potential in sensors. For example, CNCs could be co-assembled with poly (ethylene glycol) (PEG), whose structural color could be regulated by changing the fraction between CNC and PEG, and the obtained films owned responsiveness on humidity (Zhang et al. 2013). Besides, CNCs could assemble in phenol-formaldehyde resin, and then elastic membranes with structural colors that can make a response to

strain and humidity were obtained via eliminating CNCs (Khan, Giese, Yu, Kelly, Hamad and MacLachlan 2013).

Although those studies showed that flexible CNC-based membranes could be used in optical sensors, their CNC assembly structures were chiral instead of uniaxial. The reason was related to the strong interaction between CNC particles, the main of which was hydrogen bonds (H-bonds). Thus, we co-assembled CNC in poly (vinyl alcohol) (PVA), which could also form H-bonds and was flexible, and the assembly ratio between CNC and PVA was controlled to obtain a uniaxial structure of CNCs. With a morphological test from atomic force microscopy, we found that the uniaxial assembly degree of the CNC in PVA was even better than neat CNC, leading to an increase in emission quantum efficiency from 13.90–61.10%. Then, the obtained PVA/CNC membrane showed wavelength shifts in emission and excitation under strain, along with a change in photoluminescent intensity, which could be directly observed by naked eyes. The mechanism study in such a stimulation-response phenomenon suggested that the response mainly came from the change in the effective refractive index of the membrane, and the assembly ratio between CNC and PVA played a key role in increasing response sensitivity. Since the PVA/CNC co-assembly structure owned high quantum-efficiency and flexibility, it could not only be applied in the optical sensor, but also in the field of information security, like anti-counterfeiting labels and invisible patterns.

Experimental Sections

Materials

Cotton linter was obtained from Hubei Chemical Fiber Group Co., Ltd. (China). Poly(vinyl alcohol) (PVA, 1788 model with the alcoholysis degree of 87.0% – 89.0%) was purchased from Greagent (China), and sodium hydroxide (NaOH) and sulfuric acid (H_2SO_4 , 98%) were purchased from Aladdin (China).

Extraction of cellulose nanocrystals (CNCs)

The CNC was extracted from cotton linters by the acid hydrolysis with H_2SO_4 according to the previous work (Li et al. 2019). For the first step, the linters were treated with a 2 wt% NaOH solution (generally 50 g fibers for 2 L solution) for 12 h at room temperature. Then the alkali-treated fiber was filtered and washed with distilled water for about 3 times to get a neutral supernatant. After that, the acid hydrolysis (12.5 g fiber for 250 mL solution) was conducted at 45 °C using 65 wt% H_2SO_4 with mechanical stirring for 60 min. Subsequently, the suspension was quenched by diluting with about 600 mL cold deionized water, washed several times, and centrifuged at a rotation rate of 4000 rpm. Subsequently, the suspension was dialyzed until neutrality. Finally, a high concentration (3 wt%) of the CNC suspension was obtained by rotary evaporation.

Preparation of the CNC/PVA uniaxial co-assembled membranes

Firstly, 20 g of PVA was dissolved into 180 g deionized water under mechanical stirring at 95 °C for about 2 h to prepare an aqueous solution of 10 wt% PVA. Subsequently, the given amount of CNC suspension was added into the PVA solution with the magnetic stirring to gain a homogeneous suspension. After short sonication, 10 mL mixture suspension was poured into a 30 mL sample bottle, and a sliding glass was vertically inserted into the suspension, then the CNC/PVA membranes were obtained by evaporating the water at 30 °C. Based on the mass ratio of CNC and PVA in the resultant membrane, the samples were coded as CNC-X, where the number X represented the mass percentage of CNC in the total of CNC and PVA.

Characterizations

Ultraviolet and visual adsorption (UV-vis), zeta potential, photoluminescence (PL) spectra, and PL emission quantum yield analysis

UV-vis tests were carried out on a Cary Lambda 750 S spectrophotometer (PerkinElmer). Zeta potential of CNC/PVA suspension (pH = 7) was measured by a NanoBrook Omni (Brookhaven). PL spectra of CNC/PVA membranes were tested on the 5JI-004 (Hitachi) with the solid-state mode. The measurement of PL emission quantum-efficiency (EQE) was conducted with F-4500 fluorescence spectrophotometer (Hitachi). The measuring conduction was the solid-state mode.

Scanning electron microscopy (SEM) and atomic force microscope (AFM)

The fracture plane morphologies of the CNC/PVA assembled membranes were characterized by SEM using a JSM-IT300 field emission scanning electron microscope (JEOL), and the acceleration voltage was 10.0 kV. The morphologies of the membranes were carried on a Dimension Icon (Bruker). The characterization was tested by the tip of Scanasyst-air under the Scanasyst mode and by the tip of OTESPA-R3 under the Tapping mode.

Tensile tests

The tensile test was performed using a CMT6503 universal testing machine (SANS) with strain rate of tensile tests was 5 mm/min. For CNC-50 and CNC-40 membranes, they were strengthened to an elongation of 20%, 40%, 60%, 80% and till break to make the PL tests.

Thermogravimetric analysis (TGA)

The TGA test was performed using TGA 4000 (PerkinElmer). The experiments were tested under dry nitrogen purge at a flow rate of 10 mL/min from room temperature to 800 °C at the heating rate of 40 °C/min.

X-ray diffraction (XRD)

XRD was used to study the structure property of CNC/PVA co-assembly membranes before and after stretching, and it was carried out on X-Ray diffractometer (XRD-6000; Shimadzu, Japan). Cu K α radiation was operated at $\lambda = 0.154$ nm from 5° to 50° with a step speed of 2°/min.

Results And Discussions

Luminescence properties and mechanical response of CNC/PVA co-assembly membranes

Stable dispersion of cellulose nanocrystals (CNCs) in suspension is necessary for the uniaxial assembly of CNC. Table 1 shows the zeta-potential of CNC in the suspension with poly (vinyl alcohol) (PVA) with different ratios, which indicated that neat CNC suspension owned an extremely high zeta potential of -72.2 mV. As the PVA percentage increased, the zeta potential decreased but remained at a high level of > 30 mV, which indicated the suspensions were still highly stable (Kiprono et al. 2018). In order to eliminate the chiral structure, the zeta potential of the CNC dispersion should not be too high to achieve the uniaxial assembly with higher orientation. Thus, the CNC/PVA system should have better assembly potential than neat CNC.

Table 1
Zeta potential values of CNC/PVA suspension.

Samples	CNC-100	CNC-80	CNC-60	CNC-50	CNC-40	CNC-20
Zeta Potential (mV)	-72.2	-46.5	-44.3	-43.5	-42.2	-38.9

Figure 1a shows the absorption spectra of CNC/PVA co-assembled membranes. Since both cellulose and PVA had no absorption in UV and visible range, the absorption peaks around 368 nm must come from the structural color of CNC assembly. The photoluminescence (PL) spectra Fig. 1b show excitation peaks at similar wavelengths and the emission wavelengths (Em) were around 368 nm. Those results suggested that CNCs could uniaxially assemble with PVA and emit blue light under UV light.

Figure 2a and 2b proved the uniaxial assemble structure still existed in the CNC/PVA composites, but PVA took up a large volume, and it wrapped CNC around it. As seen in Fig. 2c and 2d, for the fracture surfaces of CNC-50 and CNC-40 displayed similar results, there were not apparent chiral structures, and they were both smooth. However, in Fig. 2e, CNC-100 showed a different format under the larger observation size than CNC-40 and CNC-50. It could be the large scale of chiral nematic structure though it had a high orientation in small size less than 1 μ m. This was also the reason for the EQE of the CNC/PVA uniaxial co-assembly composites were much higher than that of the neat CNC membrane.

The percentage of CNC also affects the mechanical and tensile-response properties of the CNC/PVA membranes. CNC-80 and CNC-60 showed a low elongation at break, which was 4.2% and 7.0%, respectively, when that of neat CNC membrane was less than 0.1%. Those membranes displayed no tensile responsiveness. By contrast, the elongation at the break of CNC-50, CNC-40, and CNC-20 could be more than 90%. Furthermore, CNC-50 and CNC-40 exhibited shifts in excitation wavelengths (Ex) during stretching, while CNC-20 showed little responsiveness. In detail, the Ex of CNC-50 showed an apparent blue shift when the elongation reached 40%, and it continued to decrease to 346 nm at the break, compared with the initial Ex wavelength of 368 nm, as shown in Fig. 3. The Ex of CNC-40 sample displayed similar results, and the maximal decrement of Ex wavelengths was 22 nm and 17 nm for CNC-50 and CNC-40, respectively. Emission wavelengths (Em) of CNC-50 and CNC-40 also showed a slight blue shift overall when the elongation from 0 to 90% or 94%.

Besides, the luminescence intensity also increased during the stretching. As shown in Table 2, the emission quantum-efficiencies (EQEs) of CNC-50 and CNC-40 were 48.30% and 60.60%, respectively, both of which were much higher than neat CNC uniaxial assembled membranes (13.90%) (Gan, Feng, Liu, Zheng, Li and Huang 2019). During stretching, the EQEs of CNC-50 and CNC-40 could increase to 61.10% and 63.52%, respectively, and their photoluminescent lifetime also increased slightly. Figure 4 also illustrates that the luminous intensity of CNC/PVA membranes was higher after tensile treatment.

Table 2
EQE of CNC-50 and CNC-40 before and after stretching.

Samples	lifetime (ns)	EQE (%)
CNC-40	1.26	48.30
CNC-40 at 80% elongation	1.27	61.11
CNC-50	1.18	60.60
CNC-50 at 80% elongation	1.22	63.52

Responsiveness mechanism

The mechanisms of tensile response and photoluminescent enhancement were studied with the uniaxial assembly structure of CNC as the beginnings shown in Scheme 1. CNC assembly was regarded as a dense hexagonal arrangement (DHA) in the PVA matrix (Wang et al. 2015), and the Bragg-diffraction wavelength (λ) of the uniaxially assembled CNC could be expressed by Eq. (1) (Zhu et al. 2016):

$$m\lambda = 2D \sqrt{n_{\text{eff}}^2 - \sin^2\theta}$$

1

where m is the diffraction order. For CNCs, the m should be 1 (Gan, Feng, Liu, Zheng, Li and Huang 2019). n_{eff} is the effective refractive index, D is the vertical periodicity, and θ is the incident angle.

In this work, the incident angle was 90° , so the value of $\sin^2\theta$ was 1. The refractive index of CNC and PVA were 1.534 (Shopsowitz et al. 2010) and 1.520–1.550 (Natarajan et al. 2017), respectively. Since the λ was 368 nm, the D should be 158.2 nm, which was slightly larger than the average length of CNC. The difference should be ascribed to the introduction of PVA between CNC.

After stretching, the E_x of both CNC-40 and CNC-50 firstly decreased a little at the elongation of 20%, and then showed a substantial decrement as the elongation increased from 20–40%, then steeply decrease until the break. The decrease of E_x wavelength might be from the change in D and n_{eff} . However, we found the change was mainly attributed to the n_{eff} . The n_{eff} decreased with an increasing strain due to the vacuum, which owned a lower refractive index. In byte DHA of CNC in PVA, we regarded CNC as a cylinder with a radius of r (4.5 nm), a length of L (144 nm), and a minimum vertical distance between CNC particles of e . The edge of hexagonal was coded as R . According to the thermogravimetry analysis (TGA) results in Table 3, the CNC component of CNC-50 and CNC-40 was calculated to be 64.5 wt% and 43.7 wt%, respectively, with Eq. (2) (Liu et al. 2019):

$$C = \frac{W_{\text{CNC/PVA}} - W_{\text{PVA}}}{W_{\text{CNC}} - W_{\text{PVA}}} \times 100\%$$

2

where $W_{\text{CNC/PVA}}$, W_{CNC} , and W_{PVA} were the residual weight of CNC/PVA, CNC, and PVA at 800°C , respectively. With the densities of CNC and PVA (1.56 g cm^{-3} (Giese et al. 2015) and 1.19 g cm^{-3} (Wang and Walther 2015), respectively), the volume fraction (V_{CNC}) of CNC-50 and CNC-40 should be 58.1% and 37.2%, so R could be calculated by Eq. (3):

$$R = \sqrt{\frac{\pi r^2 L}{2\sqrt{3}D \times V_{\text{CNC}}}}$$

3

The R of CNC-50 and CNC-40 were 5.36 nm and 6.70 nm, respectively, which indicated CNCs might be tightly arranged in the PVA matrix. We first assumed the D changed, which meant it must decrease during stretching to keep consistency with the decrease in λ . However, the decreasing D implied the material was shrinking, which was clearly contradicted to the tensile test conditions.

Then, we assumed the D was constant and the n_{eff} decreased during stretching due to the vacuum generation, so we could calculate the n_{eff} of stretched membranes with Eq. (4) (Zhao et al. 2012):

$$n_{\text{eff}}^2 = n_1^2 f_1 + n_2^2 f_2 \quad (4)$$

where n_1 and n_2 are the effective refractive index of PVA/CNC and vacuum, the value of n_2 is 1, and f_2 is the fraction of vacuum and air. Apparently, $f_2 = 1 - f_1$.

The results of f_1 were shown in Table 4. The Δf_1 displayed the same tendency of the change by stretching the CNC-50 and CNC-40 membranes. Those results suggested that the membrane did not gain much vacuum or air at first, so the λ nearly did not change when the elongation was smaller than 20%. By contrast, when the elongation increased further, the plastic strain of PVA led to the introduction of vacuum and air. Then the f_2 increased rapidly, and thus the E_x decreased obviously. Subsequently, with stationary stretching, the vacuum generation of CNC-50 and CNC-40 showed consistent results of Δf_1 with the change of elongation. Finally, the materials fractured and resulted in a massive change in n_{eff} , which led to a large decrease in E_x wavelength again.

Table 3
Residual weight of different CNC/PVA membranes at 800 °C.

Samples	CNC-100	CNC-50	CNC-40	CNC-20	CNC-0
Residual weight (wt%)	26.02	17.13	11.92	4.76	1.03
CNC content (wt%)	100.0	64.5	43.7	15.0	0.0

Table 4
 λ , n_{eff} , f_1 , and Δf_1 at different elongation for CNC-50 and CNC-40.

CNC-50					CNC-40				
Elongation	λ (nm)	n_{eff}	f_1	Δf_1	Elongation	λ (nm)	n_{eff}	f_1	Δf_1
20%	366	1.529	0.989	-	20%	367	1.531	0.994	-
40%	354	1.500	0.926	0.063	40%	357	1.508	0.941	0.053
60%	352	1.496	0.915	0.011	60%	355	1.503	0.931	0.010
80%	350	1.491	0.909	0.006	80%	354	1.500	0.926	0.005
90%	346	1.482	0.884	0.023	94%	351	1.494	0.910	0.016

The results were also coincident with SEM and XRD analysis. Compared with the unscratched membrane in Fig. 2c, the stretched membrane in Fig. 6a seemed to own better orientation, and the traces of vacuum during stretch could be found. Meanwhile, the CNC-40 fracture surfaces displayed similar results, but the orientation was not noticeable. The XRD results in Fig. 7a and 7b displayed a typical diffraction peaks at 2θ values of around 22.0° in all samples, which is coincident of diffraction planes of (200) in the cellulose I crystal (French 2013). The diffraction peaks at 2θ values of around 20° belong to the PVA (Kim et al. 2020). The crystallinity of CNCs can be represented by Segal crystallinity index (Crl) (French et al. 2013). Crl of CNC-40 and CNC-50 decreased from 73.73–58.86% and from 79.25–64.77% respectively after stretching, which results from the decrease of relative density of CNCs under the same scan area. On the other hand, in the stretching process, although D is constant, the parallel distance between CNCs might be smaller, because the stretching produced a shrinking perpendicular to the stretching direction (Yu et al. 2018), so the EQE showed a lift after stretching. Besides, the R of CNC-40 was larger. Thus the

EQE increase was greater than that of CNC-50. In addition, although CNC-20 was also tough, the CNC content was too low (15.0 wt%). Thus, the formation of the vacuum could be hard, and it showed little response to mechanical stimulation. These results also confirm our assumption that the decrease of the Ex wavelength and the luminescence enhancement of CNC/PVA membrane was due to the n_{eff} change should be correct.

Conclusions

Cellulose nanocrystals (CNCs) were able to uniaxial assemble to form photoluminescent membranes, but the brittleness of the material limited the application. Herein, we combined the advantages of flexible poly (vinyl alcohol) (PVA) and assembled abilities of CNCs to uniaxial co-assemble to form flexible photoluminescent membranes. In addition, we regulated the volume fraction of the two components to control the tensile property and luminescence intensity of the co-assembled membranes. The obtained composites had not only high photoluminescence quantum yield (EQE) but also gain mechanical response capacity. With the introduction of PVA, the elongation at break of the material could increase to more than 90%, and the excitation (Ex) wavelength decreased with the increase of the elongation. In addition, the EQE increased a lot compared with the neat CNC membrane, and it could further increase after stretching. We studied the mechanism of such responsiveness and constructed a close-packed hexagonal model of CNC assembly. Through the calculating, we found the decrease of Ex wavelengths was attributed to the formation of vacuum during the tensile treatment. The vacuum could change the effective refractive index (n_{eff}) and thus cause a decrease of the Bragg-diffraction wavelengths. Too little PVA in CNC/PVA composites could lead to brittle materials, while too much might result in a loss of responsiveness. The propel CNC/PVA membranes owned much higher emission intensity for the elimination of chiral structure and showed mechanical responses. Thus the flexible photoluminescent materials had the potential in anti-counterfeiting and mechanical sensing fields.

Declarations

Acknowledgements

This research is financially supported by the National Natural Science Foundation of China (51603171 and 51973175), the Project for Chongqing University Innovation Research Group (CXQT19008), the Chongqing Talent Plan for Innovation and Entrepreneurship Demonstration Team (CQYC201903243), and the Key Laboratory of Polymeric Composite & Functional Materials of Ministry of Education (PCFM201605).

Conflict of interest

The authors declare no competing financial interest.

References

1. Wu J, Niu W, Zhang S, Wu S, Ma W, Tang B (2019) A flexible and robust dual-network supramolecular elastic film with solvent resistance and brilliant structural colors *New. Journal of Chemistry* 43:11517–11523. doi:10.1039/c9nj02308a
2. Zhao Z, Wang H, Shang L, Yu Y, Fu F, Zhao Y, Gu Z (2017) Bioinspired Heterogeneous Structural Color Stripes from Capillaries *Advanced materials* 29:doi:10.1002/adma.201704569
3. Chu L, Zhang X, Niu W, Wu S, Ma W, Tang B, Zhang S (2019) Hollow silica opals/cellulose acetate nanocomposite films with structural colors for anti-counterfeiting of banknotes. *Journal of Materials Chemistry C* 7:7411–7417. doi:10.1039/c9tc01992h
4. Yang D, Liao G, Huang S (2019) Invisible photonic prints shown by UV illumination: combining photoluminescent and noniridescent structural colors. *Journal of Materials Chemistry C* 7:11776–11782. doi:10.1039/c9tc03982a
5. Echeverri M, Patil A, Xiao M, Li W, Shawkey MD, Dhinojwala A (2019) Developing Noniridescent Structural Color on Flexible Substrates with High Bending Resistance *ACS applied materials & interfaces* 11:21159–21165 doi:10.1021/acsami.9b04560
6. Wang F, Feng L, Qin Y, Zhao T, Luo H, Zhu J (2019) Dual functional SiO₂@TiO₂ photonic crystals for dazzling structural colors and enhanced photocatalytic activity. *Journal of Materials Chemistry C* 7:11972–11983. doi:10.1039/c9tc03426a
7. Zhang J, Zhu Z, Yu Z, Ling L, Wang C-F, Chen S (2019) Large-scale colloidal films with robust structural colors. *Mater Horiz* 6:90–96. doi:10.1039/c8mh00248g
8. Tong L, Qi W, Wang M, Huang R, Su R, He Z (2016) Tunable Design of Structural Colors Produced by Pseudo-1D Photonic Crystals of Graphene Oxide *Small* 12:3433–3443 doi:10.1002/sml.201600148
9. Gu M, Jiang C, Liu D, Prempeh N, Smalyukh II (2016) Cellulose Nanocrystal/Poly(ethylene glycol) Composite as an Iridescent Coating on Polymer Substrates: Structure-Color and Interface Adhesion *ACS applied materials & interfaces* 8:32565–32573 doi:10.1021/acsami.6b12044
10. Gan L, Feng N, Liu S, Zheng S, Li Z, Huang J (2019) Assembly-Induced Emission of Cellulose Nanocrystals for Hiding Information *Particle & Particle Systems Characterization* 36:1800412. doi:10.1002/ppsc.201800412
11. Shopsowitz KE, Hamad WY, MacLachlan MJ (2012) Flexible and Iridescent Chiral Nematic Mesoporous Organosilica Films. *J Am Chem Soc* 134:867–870. doi:10.1021/ja210355v
12. Guidetti G, Atifi S, Vignolini S, Hamad WY (2016) Flexible Photonic Cellulose Nanocrystal Films *Advanced materials* 28:10042–10047. doi:10.1002/adma.201603386
13. Leng J, Li G, Ji X, Yuan Z, Fu Y, Li H, Qin M, Moehwald H (2018) Flexible latex photonic films with tunable structural colors templated by cellulose nanocrystals. *Journal of Materials Chemistry C* 6:2396–2406. doi:10.1039/c7tc05523d
14. Kelly JA, Shukaliak AM, Cheung CC, Shopsowitz KE, Hamad WY, MacLachlan MJ (2013) Responsive photonic hydrogels based on nanocrystalline cellulose *Angewandte Chemie* 52:8912–8916

doi:10.1002/anie.201302687

15. Khan MK, Giese M, Yu M, Kelly JA, Hamad WY, MacLachlan MJ (2013) Flexible mesoporous photonic resins with tunable chiral nematic structures *Angewandte Chemie* 52:8921–8924
doi:10.1002/anie.201303829
16. Giese M, Khan MK, Hamad WY, MacLachlan MJ (2013) Imprinting of photonic patterns with thermosetting amino-formaldehyde-cellulose composites. *ACS Macro Lett* 2:818–821.
doi:10.1021/mz4003722
17. Khan MK, Bsoul A, Walus K, Hamad WY, MacLachlan MJ (2015) Photonic Patterns Printed in Chiral Nematic Mesoporous Resins *Angewandte. Chemie International Edition* 54:4304–4308.
doi:10.1002/anie.201410411
18. Yao K, Meng Q, Bulone V, Zhou Q (2017) Flexible and Responsive Chiral Nematic Cellulose Nanocrystal/Poly(ethylene glycol) Composite Films with Uniform and Tunable Structural Color *Advanced materials* 29:doi:10.1002/adma.201701323
19. Giese M, Blusch LK, Khan MK, Hamad WY, MacLachlan MJ (2014) Responsive mesoporous photonic cellulose films by supramolecular cotemplating. *Angew Chem* 53:8880–8884.
doi:10.1002/anie.201402214
20. Zhang YP, Chodavarapu VP, Kirk AG, Andrews MP (2013) Structured color humidity indicator from reversible pitch tuning in self-assembled nanocrystalline cellulose films. *Sens Actuators B* 176:692–697. doi:10.1016/j.snb.2012.09.100
21. Li D, Wang Y, Long F, Gan L, Huang J (2019) Solvation-Controlled Elastification and Shape-Recovery of Cellulose Nanocrystal-Based Aerogels *ACS applied materials & interfaces* 12:1549–1557
doi:10.1021/acsami.9b18569
22. Kiprono SJ, Ullah MW, Yang G (2018) Encapsulation of *E. coli* in biomimetic and Fe₃O₄-doped hydrogel: structural and viability analyses *Applied. microbiology biotechnology* 102:933–944.
doi:10.1007/s00253-017-8625-6
23. Wang B, Walther A (2015) Self-Assembled, Iridescent, Crustacean-Mimetic Nanocomposites with Tailored Periodicity and Layered Cuticular. *Structure ACS Nano* 9:10637–10646.
doi:https://doi.org/10.1021/acsnano.5b05074
24. Zhu Y, Xuan H, Ren J, Liu X, Zhao B, Zhang J, Ge L (2016) Humidity responsive self-healing based on intermolecular hydrogen bonding and metal–ligand coordination. *RSC Advances* 6:89757–89763.
doi:10.1039/c6ra11418k
25. Shopsowitz KE, Qi H, Hamad WY, MacLachlan MJ (2010) Free-standing mesoporous silica films with tunable chiral. nematic structures *Nature* 468:422–425. doi:10.1038/nature09540
26. Natarajan B, Gilman JW (2017) Bioinspired Bouligand cellulose nanocrystal composites: a review of mechanical properties *Philosophical Transactions of the Royal Society A: Mathematical. Physical Engineering Sciences* 376:20170050. doi:10.1098/rsta.2017.0050
27. Liu S, Chen Y, Liu C, Gan L, Ma X, Huang J (2019) Polydopamine-coated cellulose nanocrystals as an active ingredient in poly(vinyl alcohol) films towards intensifying packaging application potential

28. Giese M, Blusch LK, Khan MK, MacLachlan MJ (2015) Functional materials from cellulose-derived liquid-crystal. templates *Angewandte Chemie* 54:2888–2910. doi:10.1002/anie.201407141
29. Zhao Y, Xie Z, Gu H, Zhu C, Gu Z (2012) Bio-inspired variable structural color materials. *Chem Soc Rev* 41:3297. doi:10.1039/c2cs15267c
30. French AD (2013) Idealized powder diffraction patterns for cellulose polymorphs *Cellulose* 21:885–896 doi:10.1007/s10570-013-0030-4
31. Kim J, Jayaramudu T, Zhai LD, Kim HC, Agumba DO (2020) Preparation of Cellulose Nanocrystal-Reinforced Physical Hydrogels for Actuator Application *Crystals* 10:doi:10.3390/cryst10110969
32. French AD, Cintron MS (2013) Cellulose polymorphy, crystallite size, and the Segal Crystallinity Index *Cellulose* 20:583–588 doi:10.1007/s10570-012-9833-y
33. Yu Z, Li B, Chu J, Zhang P (2018) Silica in situ enhanced PVA/chitosan biodegradable films for food packages *Carbohydrate polymers* 184:214–220 doi:10.1016/j.carbpol.2017.12.043

Figures

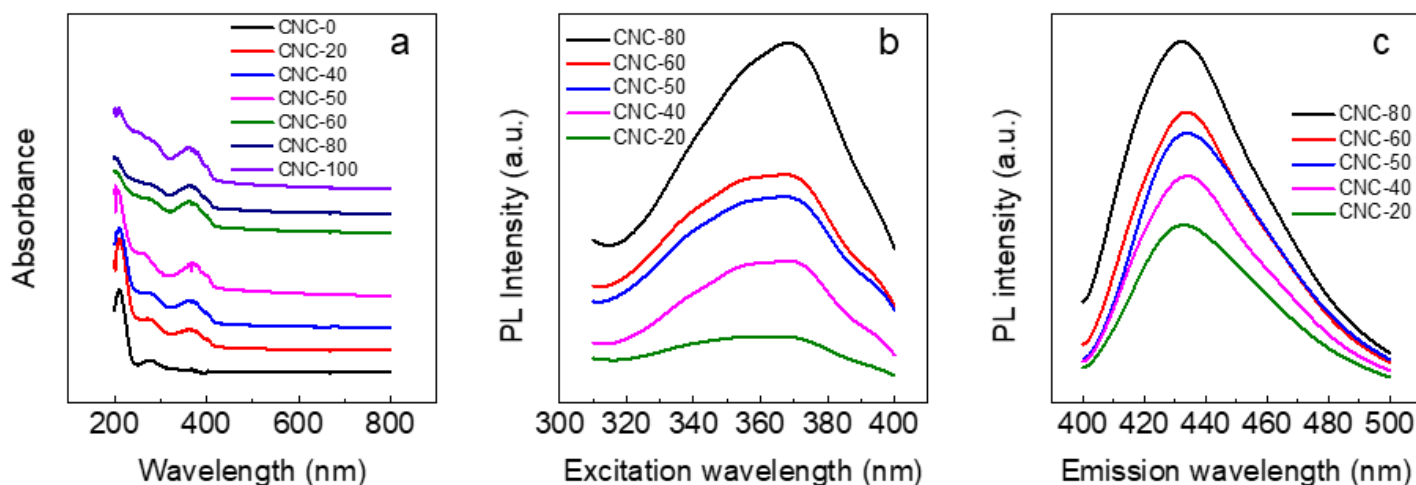


Figure 1

(a) UV-vis spectra, (b) excitation and (c) emission spectra of CNC/PVA samples with different CNC content.

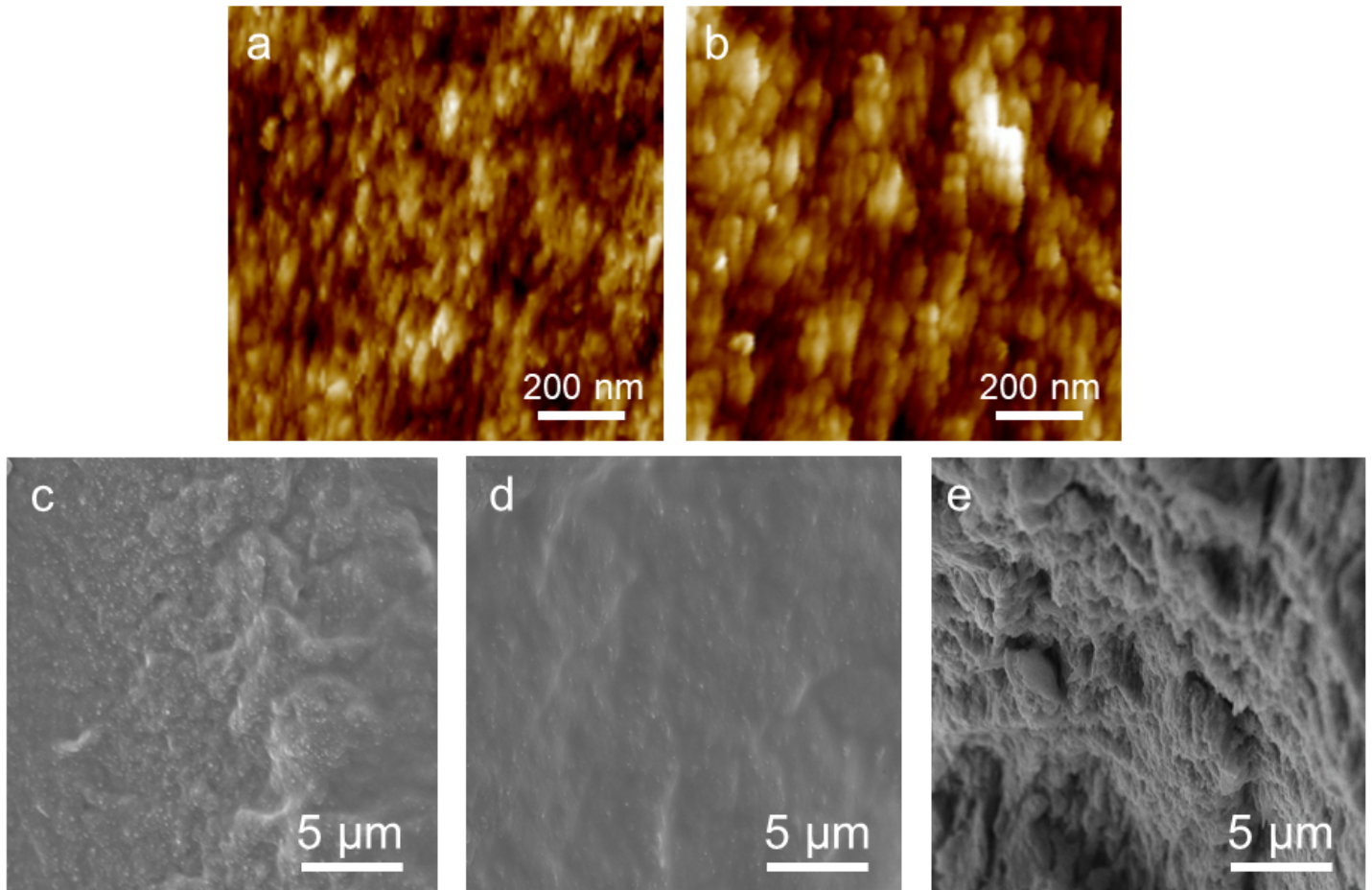


Figure 2

AFM images of (a) CNC-50 and (b) CNC-40, and fracture surfaces SEM images of (c) CNC-50, (d) CNC-40, and (e) CNC-100.

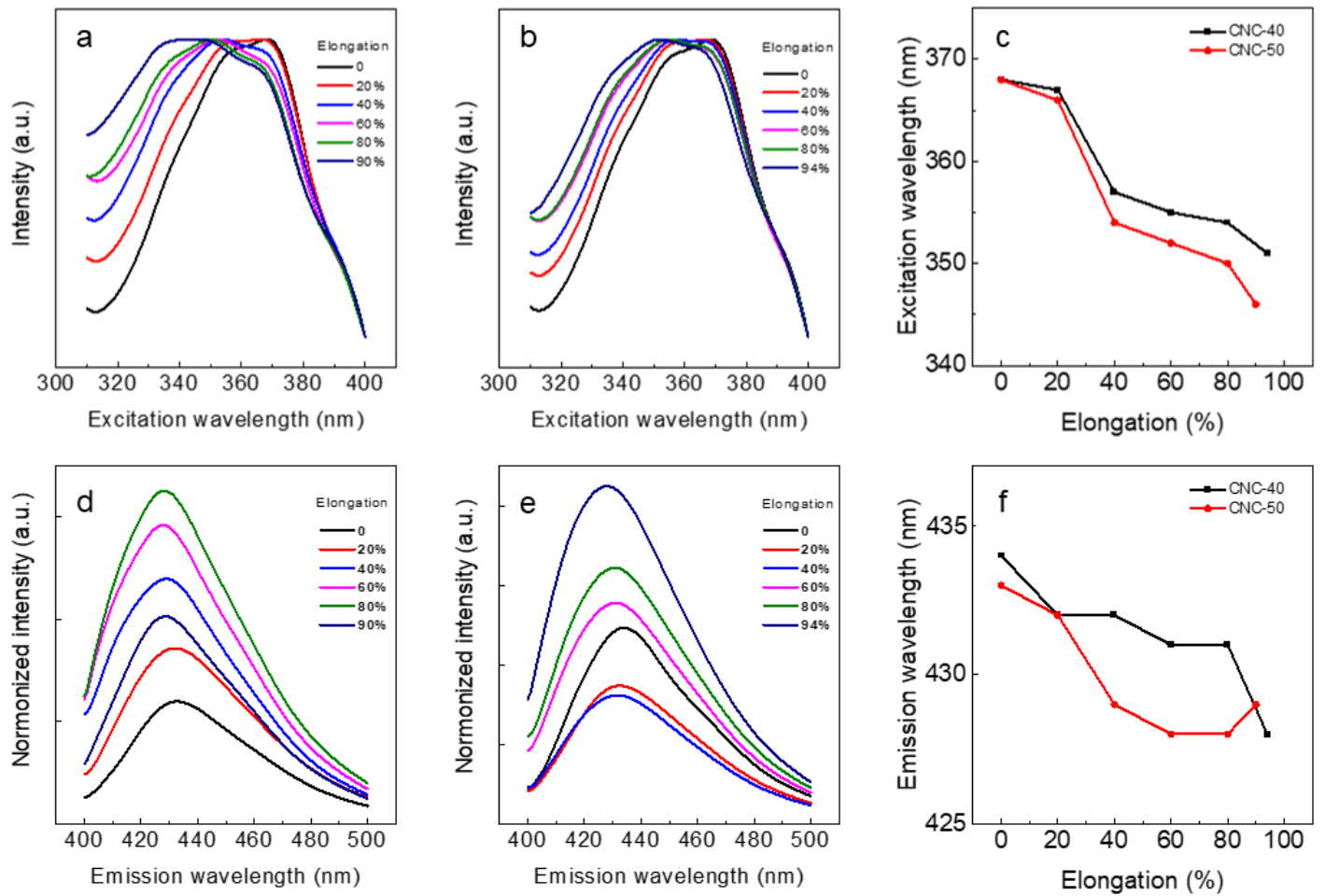


Figure 3

Intensity of excitation spectra for (a) CNC-50 and (b) CNC-40, emission spectra for (d) CNC-50 and (e) CNC-40 at different elongations; (c) and (f) line chart of excitation wavelengths and emission wavelength along with elongations for CNC-50 and CNC-40.

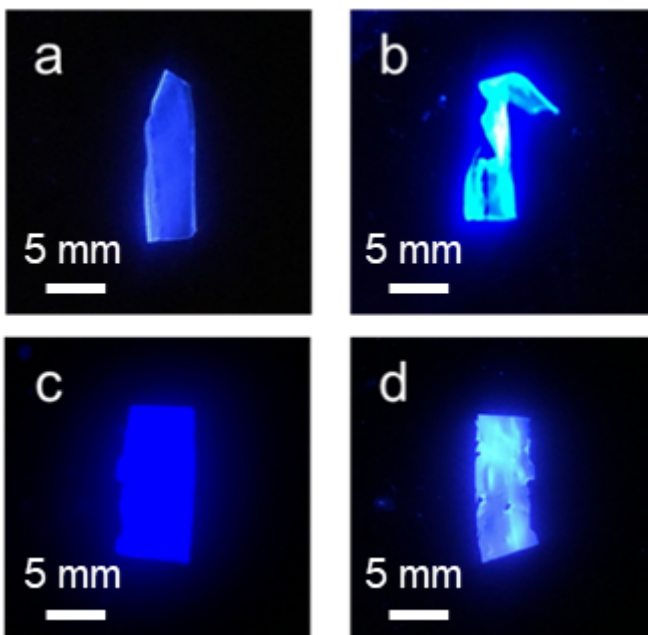


Figure 4

(a) CNC-50, (c) CNC-40 membrane and (b) CNC-50, (d) CNC-40 membrane after stretching under 365 nm UV light

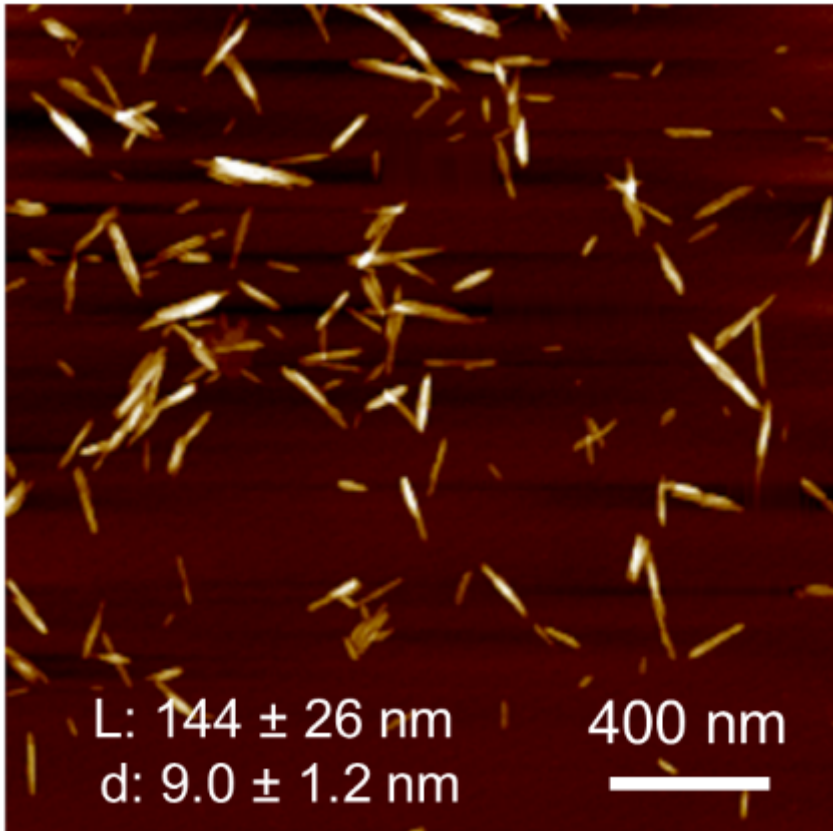


Figure 5

AFM image of CNCs prepared by 10 μL 0.001 wt% dispersion.

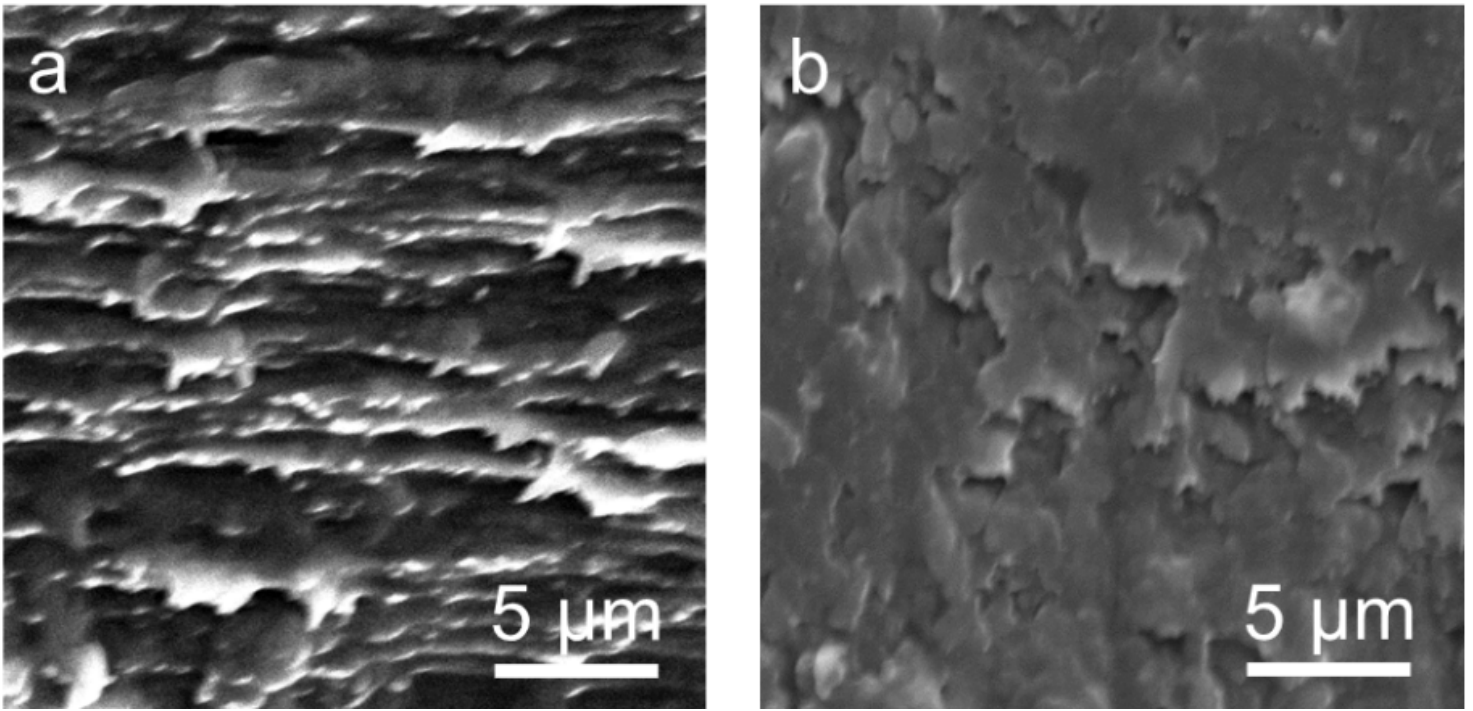


Figure 6

Fracture surfaces SEM images of stretched (a) CNC-50 and (b) CNC-40.

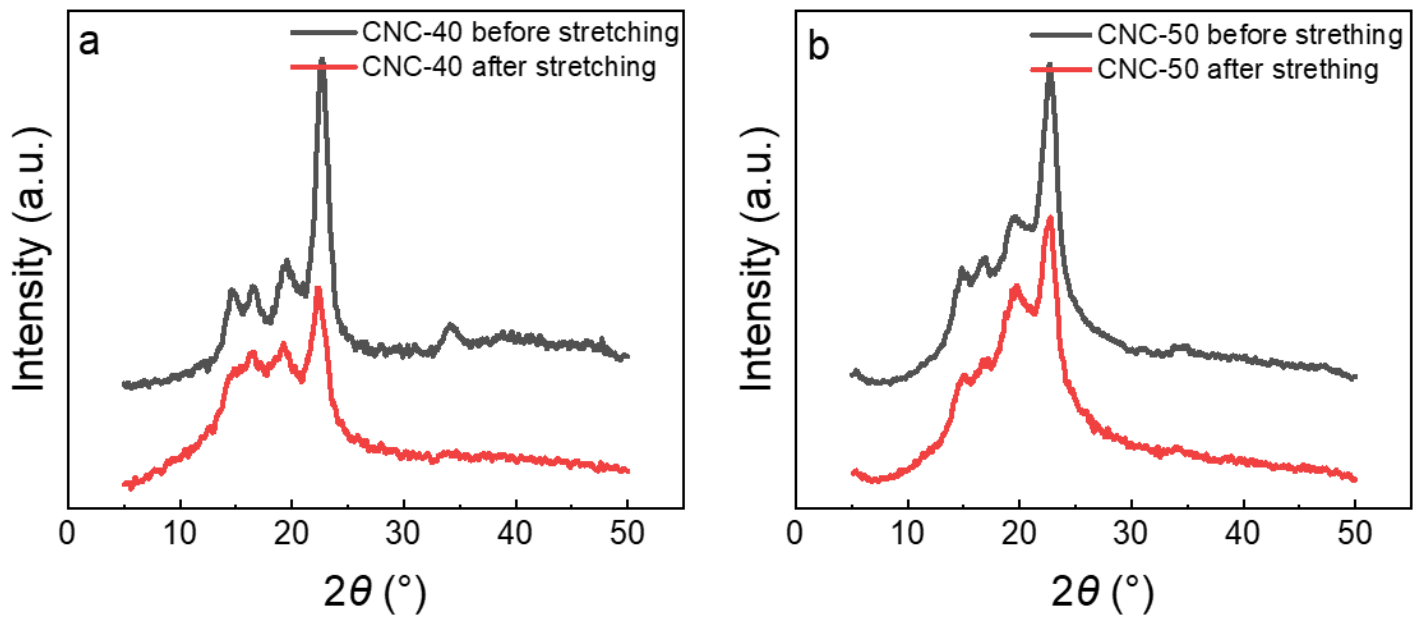


Figure 7

XRD pattern of (a) CNC-40 and (b) CNC-50 before and after stretching.

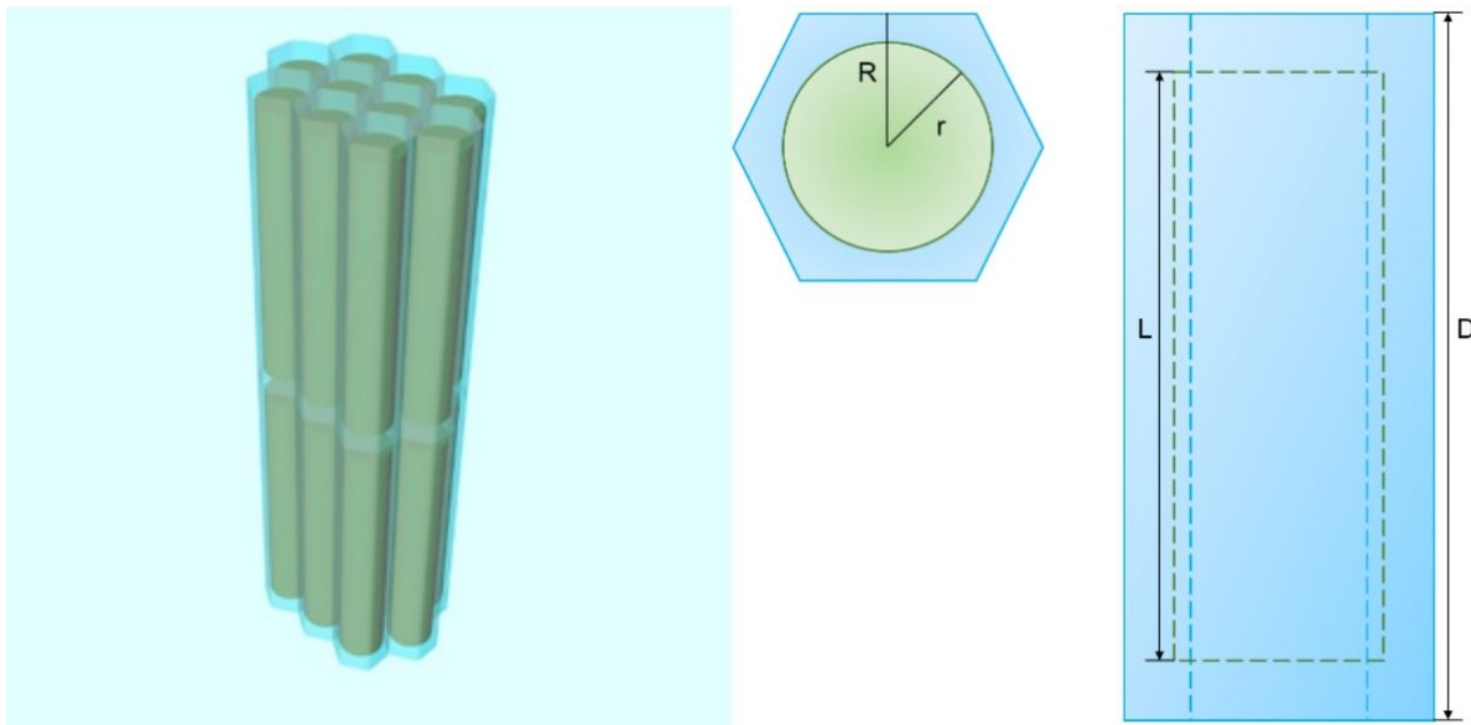


Figure 8

Scheme 1. Schematic diagram of the assembled structure of CNC/PVA materials.

Supplementary Files

This is a list of supplementary files associated with this preprint. Click to download.

- [SupportingInformation.docx](#)